Living plastics from plasticizer-assisted thermal molding of silk protein

Check for updates

Yushu Wang[1], Junqi Wu[1], Emily J. Hartzell[1], Weiguo Hu [2], Reddhy Mahle[1], Xinxin Li[1], Ying Chen [1], Jugal Kishore Sahoo [1], Cameron Chan [3], Brooke N. Longo[1], Charlotte S. Jacobus[1], Chunmei Li [1] ✉ & David L. Kaplan [1] ✉

The pursuit of materials, particularly plastics, with a minimal ecological footprint throughout their circular lifecycle, is crucial for advancing sustainable materials development. Living materials composed of embedded yet active organisms can leverage endogenous biotic resources to achieve functional materials that align with sustainability goals. However, current living material systems face challenges such as weak mechanical properties, limited environmental adaptability, and restricted cellular functionality. In this study, we propose an approach to sustainable living materials by incorporating active organisms into silk-based plastics through a plasticizer-assisted thermal molding process. We investigate the mechanism of structure formation in these materials, correlating manufacturing performance to the resulting secondary structure. These silk-based plastics provide a protective matrix for probiotics, ensuring their survival through the harsh gastrointestinal tract and enhancing intestinal delivery. Similarly, soil rhizobacteria encapsulated within the plastics exhibit long-term protease activity, accelerating plastic degradation upon soil exposure. This work demonstrates the potential of sustainable plastics as a form of living materials, where active organisms are processed, entrapped, retain metabolic functions, and are protected in harsh environments.

Microorganisms such as bacteria, fungi, and algae offer the unique advantages of self-replication and genetic programmability, making them ideal candidates for performing various regulatory and functional tasks[1]. With the advancement of high-throughput computational analysis, microorganisms are now employed as eco-friendly alternatives to corrosive chemicals for degrading polymer plastics or as biominers for extracting and purifying rare-earth metals from electronic waste[2–5]. Efforts to protect and harness microbial functions have led to the integration of active microorganisms into polymer matrices, establishing the foundation of living material systems, in contrast to conventional, non-replenishable, abiotic materials[6–9]. Living materials possess programmable features such as self-healing, regeneration, and

cleaning, while leveraging biological resources to continuously produce functional outputs[10–15].

Despite the advantages of living materials, several limitations hinder their broader application. Many microorganisms require specific laboratory media for effective proliferation, which restricts their cultivation, storage, and utility. Additionally, most living material systems rely on hydrogel, aerogel, and film matrices, which generally exhibit low mechanical strength, limiting their suitability for practical applications that require more robust materials[16–20]. Consequently, there is a growing need to develop living material systems that preserve microbial viability while maintaining functionality and stability for long-term use in diverse environments. However, integrating living

[1]Department of Biomedical Engineering, Tufts University, Medford, MA 02155, USA. [2]Department of Polymer Science & Engineering, University of Massachusetts, Amherst, MA 01003, USA. [3]Department of Bioengineering, Northeastern University, Boston, MA 02115, USA. ✉e-mail: chunmei.li@tufts.edu; david.kaplan@tufts.edu

microorganisms into dense and durable material formats remains challenging.

Silk fibroin protein extracted from *Bombyx mori* cocoons is an ideal candidate for living material systems due to its biocompatibility, low immunogenicity, biodegradability, and tunable mechanical properties[21–25]. The traditional utilization of silk fibroin (hereafter termed silk) is to process it into diverse material forms, such as films, fibers, and hydrogels in aqueous conditions; however, the silk solution used for these processes has limited stability and storage capability[26–31]. An alternative strategy to extend the shelf-life of silk is to generate amorphous powders with subsequent molding at temperatures up to 145 °C, producing dense, plastic-like materials with high crystallinity and improved machinability[32]. However, the elevated temperatures used in thermoplastic molding can compromise the viability of biological components, presenting a significant challenge to the development of robust living material systems.

Probiotics are essential for balancing the intestinal microbiome, but they often struggle to survive the harsh conditions of the gastrointestinal tract when administered externally. Moreover, commercial enteric-coated capsules frequently provide inadequate protection, resulting in substantial loss of probiotic viability during storage and transport[33–35]. Additionally, recent research on enzyme-incorporated plastics and genetically engineered spores in living plastics has shown promise for plastic degradation, though these methods remain complex, costly, and resource-intensive[36–38]. Silk-based living materials offer a promising solution by creating a protective shell around encapsulated microorganisms, ensuring their resistance to environmental stress and enhancing their viability and functionality remaining.

Here, we show a mild plasticizer-assisted molding approach of silk powders at 60 °C to prepare plastics with structural stability. This method mitigates high-temperature limitations and enables tuning of mechanical properties, balancing stiffness and toughness through modulation of protein conformational transitions. Our approach facilitates on-demand manufacturing from silk powders, addressing stability concerns associated with solution processing. Experimental and simulation results reveal the role of plasticizers during molding, elucidating relationships between structural transitions,

physicochemical properties, and microbial functions. Furthermore, this plasticizer-assisted molding method allows for the integration of living microorganisms into highly crystalline silk plastics, enhancing both microbial viability and long-term stability for various applications (Fig. 1). We demonstrate the potential of silk plastics as protective matrices for encapsulated probiotics, ensuring their survival through gastrointestinal conditions. Additionally, we incorporate naturally occurring soil rhizobacteria for silk degradation within soil, offering a sustainable and economical alternative for degradable plastics with potential as a biofertilizer.

Results

Transparent and flexible silk plastics with variable shapes were produced via a plasticizer-assisted thermal molding process. As shown in Fig. 2a, the lyophilized silk powder as the raw materials was loaded into predesigned molds after water mist plasticization, followed by compressing the powder at 60 °C at 632 MPa. The use of free water as the plasticizer enhanced the mobility of the amorphous silk protein chains, promoting the transition from amorphous to crystalline-dominated structures with a higher β-sheet content[32,39]. Numerous studies have demonstrated that ^{13}C solid-state nuclear magnetic resonance (SSNMR) is highly effective for analyzing structural transitions in silk proteins under dry conditions, offering advantages over other spectroscopic techniques like Raman, infrared radiation, and circular dichroism[40–44]. In this study, SSNMR was used to identify and quantify conformational changes induced by plasticizer-assisted thermal molding. Structural forms and proportions were analyzed in silk powder, water-plasticized silk powder containing 20% water (20% WSP, confirmed by thermogravimetric analysis (TGA)), and 20% WSP molded at 60 °C (WS/60 °C) (Fig. 2b, c, and Supplementary Fig. 1). Degummed native silk fibers were used as a control (Supplementary Fig. 2). The SSNMR spectra of the samples are presented in Fig. 2b, showing main signals for the Cα and Cβ carbons of Ala and Ser, Gly Cα, and C = O peaks. Deconvolution analyses of these peaks are provided in Fig. 2c and Supplementary Fig. 2. Based on previous studies[40,41], peaks at 20.3, 49.6, 55, 64.5, 169, and 172.7 ppm were attributed to β-sheet conformations of silk, while other signals corresponded to
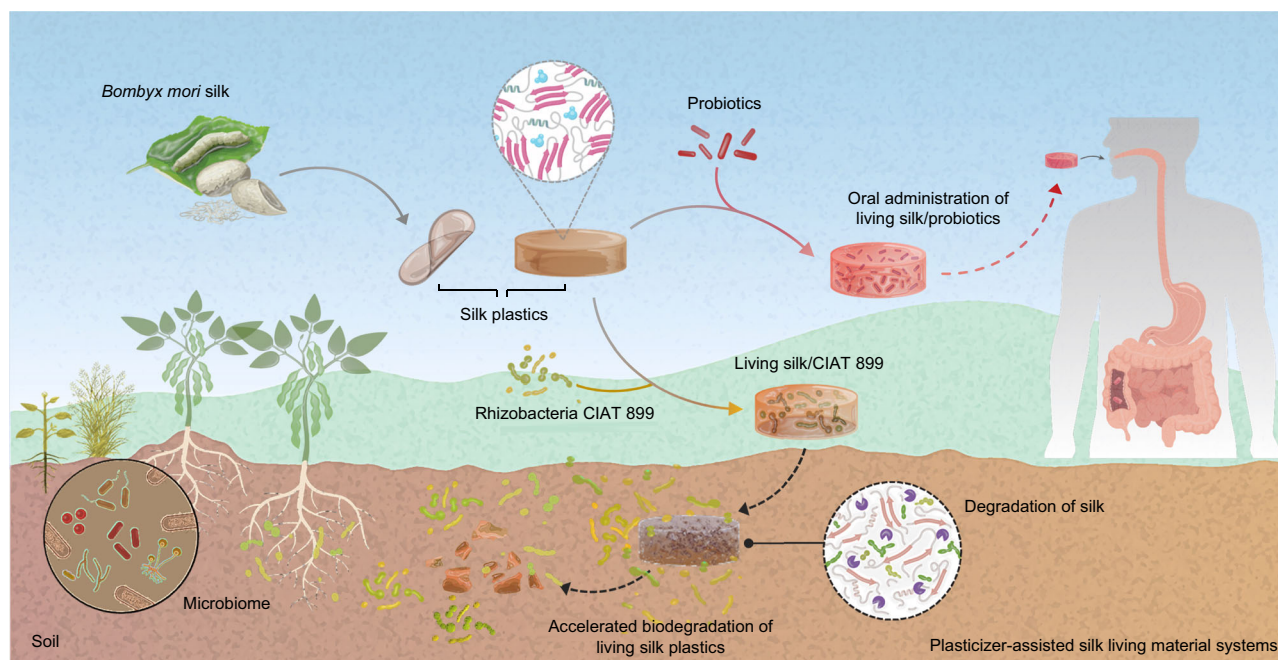

Fig. 1 | Conceptual schematic illustration of a sustainable living material system with silk plastics prepared via plasticizer-assisted thermal molding. This system is adaptable for various applications, including in vivo probiotic delivery and lifecycle soil degradation, as demonstrated in this study. Figure created with BioRender.com released under a Creative Commons Attribution-NonCommercial-NoDerivs 4.0 International license.
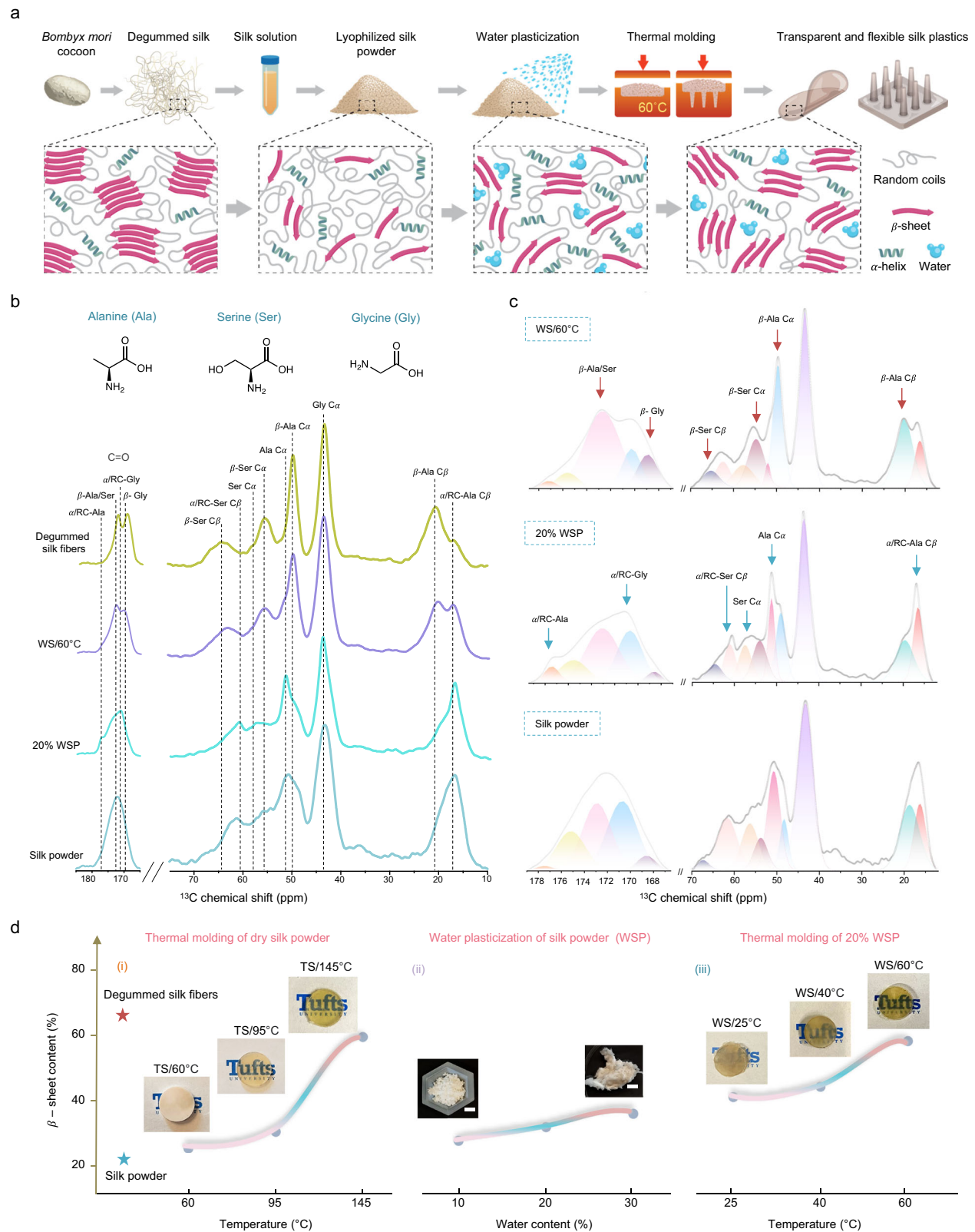
Fig. 2 | Fabrication process and conformational transitions of silk plastics.
a Schematic illustration of the fabrication steps for silk plastics using plasticizer-assisted thermal molding. **b** Solid-state ^{13}C NMR (SSNMR) spectra and (**c**) structural deconvolution analyses of silk powder, 20% WSP, WS/60°C, and degummed silk fibers. **d** Comparison of β-sheet content in silk plastics produced under various conditions, including thermal molding of silk powder from 60°C to 145°C, water-plasticized silk powder with varying water content, and molding of 20% WSP from 25°C to 60°C. Photographs in (i) and (iii) depict silk plastics with a diameter of 10 mm, and scale bars in (ii) represent 10 mm.

random coil or silk I-like structures. A summary of chemical shifts, residue assignments, and structural forms for SSNMR is provided in Table S1.

Plasticization of silk powder resulted in a narrowing of the peak at 16.6 ppm and a pronounced shoulder at 177.1 ppm, indicating a reduction in silk I-like forms and a shift towards β-sheet structures. Thermal molding of the plasticized silk at 60 °C induced significant structural transitions to the silk II form, evidenced by an increased fraction of peaks associated with β-sheets. These transitions were further quantified by deconvolution of the SSNMR spectra, comparing samples molded at different temperatures, with and without plasticization (Fig. 2d and Supplementary Figs. 3 and 4). A summary of the observed conformational transitions is provided in Table S2. Silk powders molded without plasticization exhibited limited increases in β-sheet content at 60 °C and 95 °C (TS/60 °C and TS/95 °C), with substantial increases only observed at 145 °C (TS/145 °C) (Fig. 2d, i). In contrast, plasticization with 20% water facilitated the transition from amorphous to silk I structure, and subsequent thermal molding at 60 °C led to a transition from silk I to silk II, with β-sheet content approaching that of degummed silk fibers (Fig. 2d ii, iii).

Fourier-transform infrared spectroscopy (FTIR) analysis corroborated the SSNMR findings, revealing a shift in the amide I region from 1645 cm^{-1} to 1625 cm^{-1}, indicating the formation of β-sheet in WS/60 ° during plasticizer-assisted thermal molding (Supplementary Fig. 5). To further explore the correlation between thermal stability and structural transitions, differential scanning calorimetry (DSC) and TGA were performed. Endothermic peaks below 100 °C were attributed to water loss, while exothermic peaks indicated non-isothermal crystallization in lyophilized 20% WSP, TS/60 °C, and silk powder. These DSC results suggest that the crystallization temperature increased following plasticization. However, no exothermic peak was observed in WS/60 °C, suggesting effective β-sheet crystallization and stabilization of the silk material, which prevented further crystallization during DSC scanning (Fig. 3a and Supplementary Fig. 6a)[45,46]. Consequently, the crystallization affinity followed the order WS/60 °C > 20% WSP > TS/60 °C > silk powder. The TGA curves of the lyophilized WS/60 °C, 20% WSP, TS/60 °C, and silk powder samples showed a consistent trend with the DSC results, indicating that WS/60 °C, with its high β-sheet crystallization, exhibited enhanced thermal stability and the lowest weight loss among the samples (Fig. 3b and Supplementary Fig. 6b).

X-ray diffraction (XRD) results provided further insight into the conformational transitions of the silk plastics. In amorphous silk powder, a broad peak at 19.4 ° was observed, while degummed silk fibers, used as a reference for silk II, exhibited characteristic peaks at 9.4 ° and 20.5 °. The 20% WSP spectrum showed a peak at 12.2 °, confirming the transition from an amorphous to a silk I structure facilitated by water plasticization. Subsequent molding at 60 °C promoted the crystallization of silk II, as indicated by the peak at 20.5 ° in the WS/60 °C sample (Fig. 3c and Supplementary Fig. 7)[47]. Scanning electron microscopy (SEM) images illustrate the microstructural transformation in these silk plastics (Fig. 3d). The initial silk powder consisted of loose particles, which partially fused during plasticization, forming sheet-like and fibrous structures in the 20% WSP. In the WS/60 °C, smooth and flat surfaces were observed in the SEM images, indicating that the thermal molding process led to further compaction and fusion, creating a homogeneous structure from the amorphous silk particles.

To broaden the applicability of plasticizer-assisted thermal molding, additional plasticizers, such as glycerol and a combination of water and glycerol, were tested for their effects on silk structural transformations. Characterizations using SSNMR, FTIR, and XRD (Supplementary Figs. 8-13) demonstrated that glycerol induced similar structural transitions in silk, confirming its potential as an effective plasticizer for thermal-molding silk plastic production.

Molecular dynamics (MD) simulations were conducted to further elucidate the crystalline transitions during plasticization and thermal molding. Models for silk powder, 20% WSP, TS/60 °C, and WS/60 °C were constructed, and dynamic secondary structural changes were analyzed over 200 ns simulations (Supplementary Fig. 14). The results indicated that the 20% WSP and WS/60 °C models exhibited more stable and extensive secondary structure formation compared to silk powder and TS/60 °C. Representative snapshots from the simulations (Fig. 3e and Supplementary Fig. 15 a, b) further reflected these structural trends. The average contents of β-sheets, helices, random coils, and other intermediates were quantified over the 200 ns simulation trajectories (Fig. 3f, g, h and Supplementary Fig. 15c). Compared to silk powder and TS/60 °C, the 20% WSP and WS/60 °C models exhibited reduced proportions of random coils and higher levels of helical and β-sheet content, respectively. These results demonstrated that the structural transitions in 20% WSP and WS/60 °C were driven by the transformation of metastable random coils into more stable, ordered secondary structures, supporting the experimental findings. Overall, the simulation results demonstrate that plasticizer-assisted thermal molding effectively stabilizes the silk structure by promoting the transitions from random coils and helical configurations to β-sheet-dominated silk II structures at lower temperatures.

Mechanical properties are crucial for silk plastics. Water molecules can improve protein chain mobility, providing flexibility to the plastics materials, which allowed for the WS/60 °C to be very pliable (Fig. 4a), and also capable of fabrication into micropillars with micron-scale resolution (Fig. 4b). In addition to this flexibility, the high crystallinity in dehydrated silk plastics increased stiffness, allowing for machining into parts such as bone screws and lenses (Fig. 4c). Tensile testing of WS/60 °C showed an increase in tensile modulus from 0.35 to 1.08 GPa in the β-sheet-dominated dry WS/60 °C compared to TS/60 °C (Supplementary Fig. 16a, b). In contrast, the hydrated WS/60 °C exhibited greater extensibility, reaching a maximum tensile strain of 20% and an average tensile toughness of 1.62 MJ·m^{-3}, due to the increased mobility of amorphous protein chains (Supplementary Fig. 16c). This balance of stiffness and ductility in silk plastics offers tunable mechanical properties through plasticizer-assisted thermal molding.

The biocompatibility of silk plastics was evaluated through both in vitro and in vivo studies. In vitro assessments involved culturing C2C12 cells on silk micropillar substrates with a height of 200 μm and radius of 200 μm, spaced 250 μm apart. Over 2 weeks, cell activity and immunofluorescence imaging via confocal laser scanning microscopy showed robust cell attachment and continuous proliferation, compared to control silk micropillars without cells (Supplementary Fig. 17). Myotube formation, marked by MF20 labeling, further indicated cell differentiation and confirmed the non-cytotoxic properties of the silk micropillars (Fig. 4d).

In vivo biocompatibility was assessed through subcutaneous implantation of WS/60 °C in mice for 4 weeks. Hematoxylin and eosin (H&E) staining showed a decrease in the thickness of inflammatory cell layers surrounding the implant over 28 days (Fig. 4e, g and Supplementary Fig. 18). Masson's trichrome (MT) staining revealed a thin fibrous capsule around the implant at 28 days post-implantation (Fig. 4e). In addition, the in vivo biocompatibility of the WS/60 °C was assessed through immunofluorescence staining of markers for myofibroblasts (α-smooth muscle actin (α-SMA)), macrophages (CD68), and collagen type I (COL- I) (Fig. 4f, h)[48–51]. The increased expression of α-SMA at 28 days post-implantation suggests the formation of myofibroblast, which is essential for producing and contracting the extracellular collagen matrix around the implants. COL-I staining showed minimal collagen encapsulation around WS/60 °C and no visible fluorescent signal after implantation. This limited collagen accumulation facilitates mass transfer between the host tissue and the implanted material. Macrophage involvement in the foreign body response
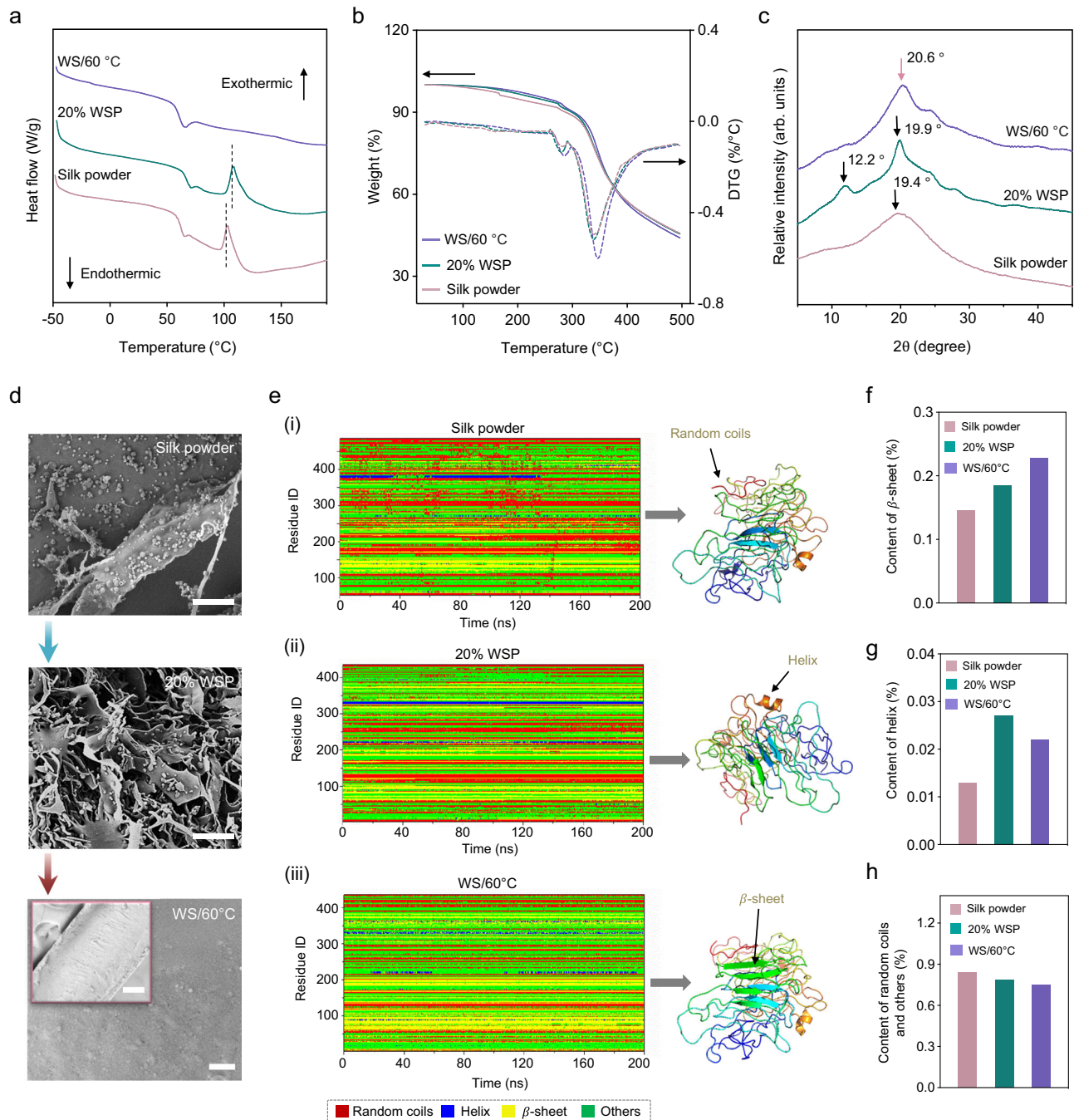
Fig. 3 | Mechanism of silk structure evolution. a DSC, (**b**) TGA, (**c**) XRD, and (**d**) SEM images of silk powder, 20% WSP, and WS/60 °C. In SEM images: scale bars are 10 μm for silk powder and 20% WSP, 500 nm for WS/60 °C, and 200 μm for WS/60 °C insert. **e** Trajectory plots of silk sequences during 200 ns simulations and representative snapshots of simulated protein structures for (i) silk powder, (ii) 20% WSP, and (iii) WS/60 °C. Quantitative analyses of protein structures, including (**f**) β-sheet, (**g**) helix, and (**h**) random coils and intermediates for simulated models of silk powder, 20% WSP, and WS/60 °C.

was evidenced by CD68-positive cells and foreign body giant cells (FBGC) at the implant-tissue interface, with elevated levels observed after 28 days compared to 14 days (Supplementary Fig. 19). These findings indicate that the implant induced a standard foreign body response, with the host attempting to degrade and remodel the implant during this phase. Based on H&E, MT staining, and immunofluorescence analyses, WS/60 °C elicited a minimal inflammatory response and no physiological toxicity after 28 days, confirming the in vivo biocompatibility of silk plastics.

Probiotics play a critical role in digestion, metabolism, and immune regulation, but their viability is often compromised during oral administration due to the harsh conditions of the gastrointestinal tract, including low pH, digestive enzymes, and bile salts[33,52,53]. In this study, *Escherichia coli* Nissle 1917 (EcN) was used as a model probiotic and incorporated into silk plastics with high β-sheet crystallinity to create a living material system for active bacterial delivery, followed by an evaluation of its protective efficacy (Fig. 5a, b)[54]. For ease of identification, EcN was transformed with the red fluorescent protein (RFP) gene (REcN), providing the bacteria with a distinct cherry color detectable through fluorescence imaging (Supplementary Fig. 20). SEM images of the lyophilized silk/REcN powder revealed rod-shaped REcN encapsulated within a silk coating prior to molding, with more
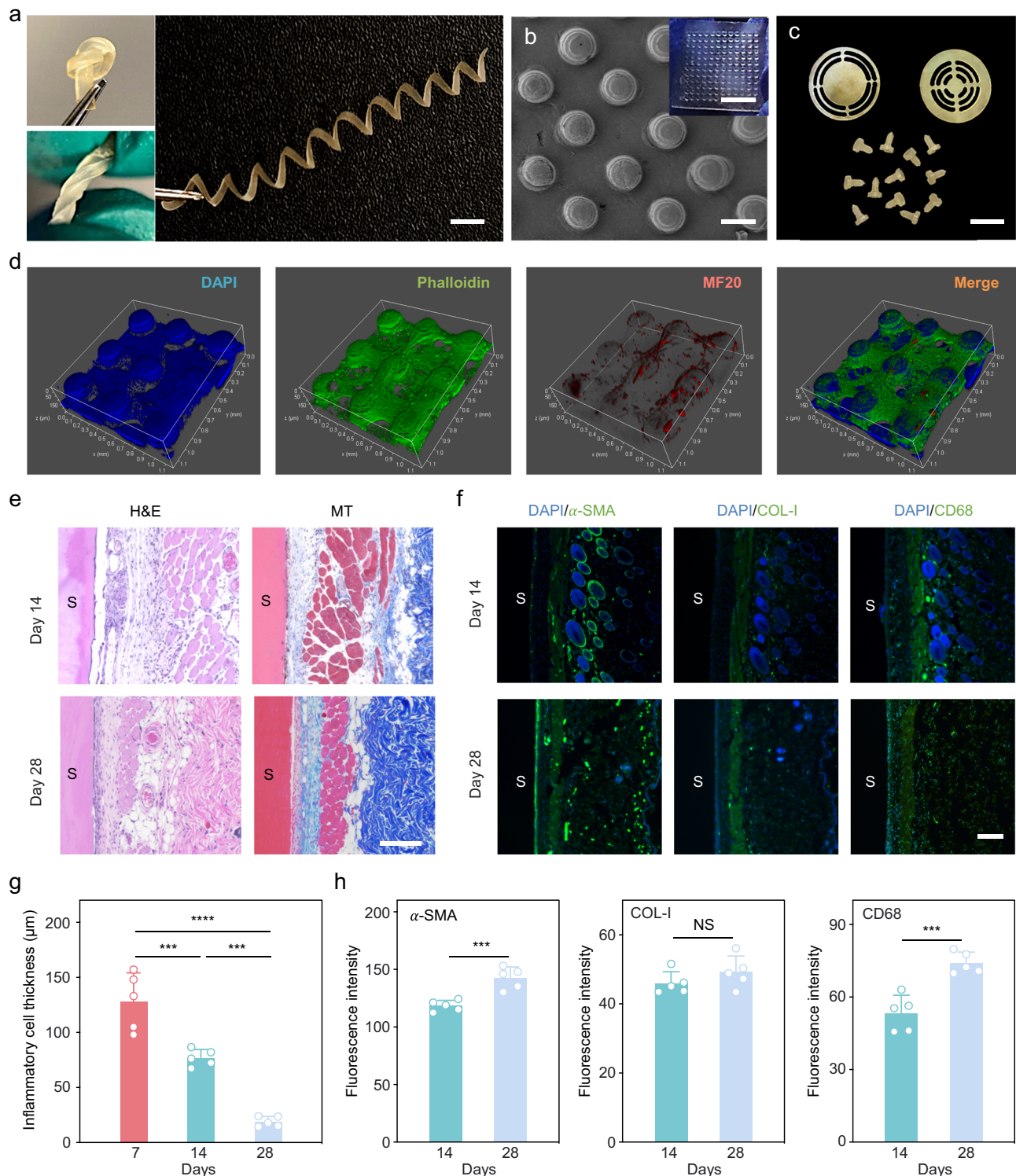
Fig. 4 | Manufacturing properties and the biocompatibility of silk plastics.
a Photographs of flexible WS/60 °C with folding, twisting, and bending designs (Scale bar: 10 mm). **b** SEM image of a WS/60 °C micropillar (Scale bar: 200 μm) with inset showing the micro-scale machining resolution of the silk plastics (Scale bar: 5 mm). **c** Photographs of complex designs machined from dehydrated WS/60 °C (Scale bar: 10 mm). **d** 3D fluorescence microscopy images of C2C12 cells cultured on WS/60 °C micropillars. **e** Representative hematoxylin and eosin (H&E) staining (nuclei in dark blue, cytoplasm in pink) and Masson's trichrome (MT) staining (collagen in blue, nuclei in black, and cytoplasm in red) of tissues surrounding WS/60 °C implants after 14- and 28-days post-implantation (n = 5 biological independent replicates) (Scale bar: 200 μm). **f** Immunofluorescence staining of paraffin

sections for α-SMA (green), COL-I (green), and CD68 (green), counterstained with DAPI (blue) (n = 5 biological independent replicates) (Scale bar: 200 μm).
g Quantification of the thickness of inflammatory cell layer around implants over time based on H&E staining (n = 5 biological independent replicates, $P = 7 \times 10^{-4}$ (day 7 vs. day 14), $P < 0.0001$ (day 7 vs. day 28), $P = 2 \times 10^{-4}$ (day 14 vs. day 28)).
h Signal density quantification in the fibrous layer surrounding the implanted WS/60 °C (n = 5 biological independent replicates, $P = 9 \times 10^{-4}$ (α-SMA), $P = 0.2404$ (COL-I), $P = 6 \times 10^{-4}$ (CD68)). "S" in (**e**) and (**f**) indicates sample locations. All data presented as mean values ± standard deviations. Statistical analysis: One-way ANOVA with Tukey's multiple comparisons in (**g**) and two-tailed unpaired t-test in (**h**) (***$P \leq 0.001$, ****$P \leq 0.0001$, NS: not significant).
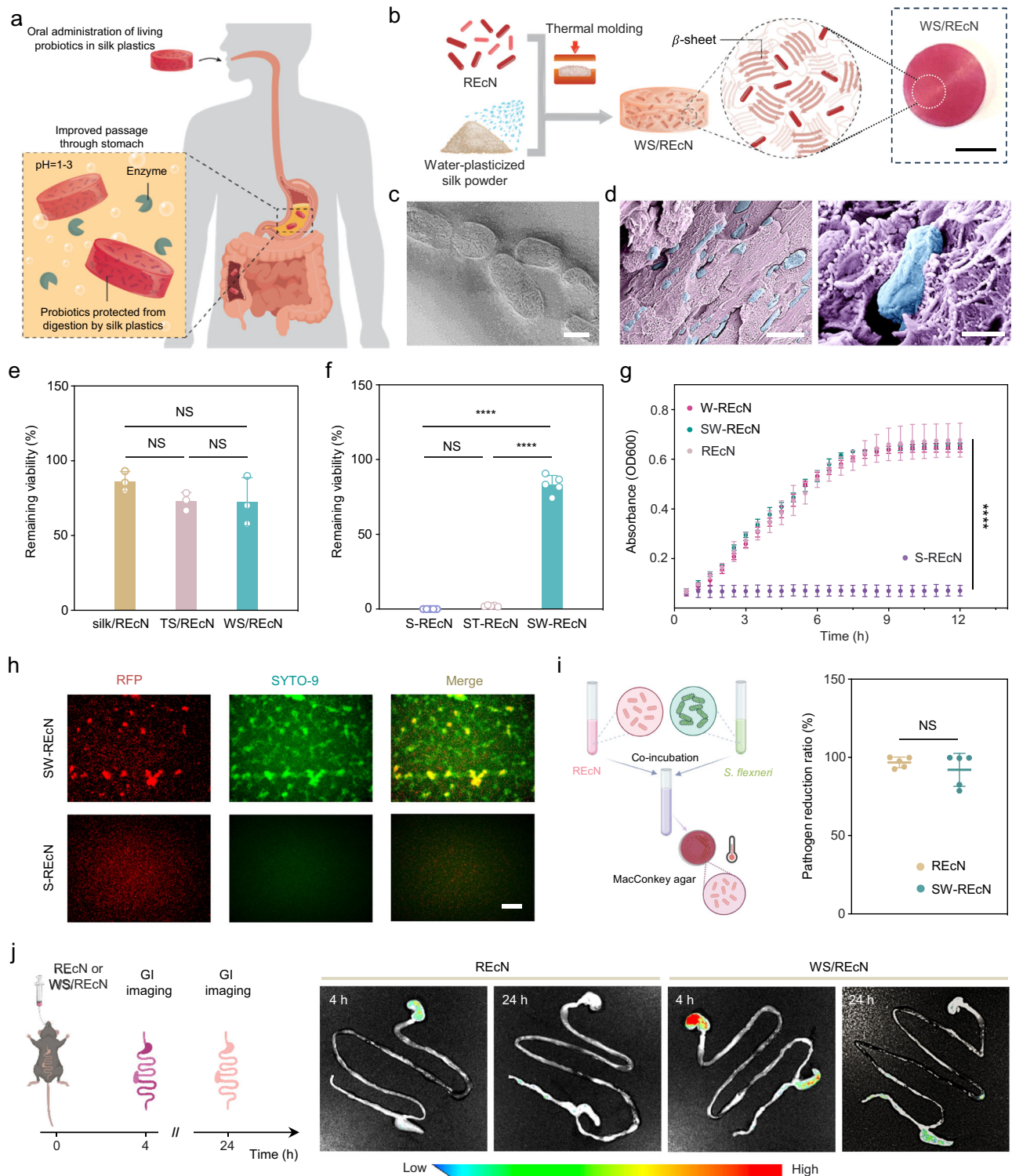
Fig. 5 | Protection of probiotics during gastrointestinal tract with silk-based living materials. a Schematic of oral delivery of REcN encapsulated in silk plastics for enhanced probiotic viability through the digestive system. **b** Photograph of WS/REcN and schematic illustrating REcN embedded within a protective, high-crystallinity silk shell (Scale bar: 5 mm). **c** SEM images of silk/REcN powders (Scale bar: 500 nm). **d** SEM images of WS/REcN (left) and individual REcN embedded in silk (right) (Scale bars: 5 μm left, 500 nm right). **e** Remaining viability of REcN from silk/REcN, TS/REcN, and WS/REcN ($n = 3$ independent replicates, $P = 0.3421$ (silk/REcN vs. TS/REcN), $P = 0.3261$ (silk/REcN vs. WS/REcN), $P = 0.9991$ (TS/REcN vs. WS/REcN)). **f** Remaining viability of S-REcN (SGF + SIF-treated REcN), ST-REcN (REcN released from SGF + SIF-treated TS/REcN), and SW-REcN (REcN released from SGF + SIF-treated WS/REcN) ($n = 5$ independent replicates, $P \leq 0.0001$ (SW-REcN vs. ST-REcN), $P \leq 0.0001$ (SW-REcN vs. S-REcN), $P = 0.6245$ (S-REcN vs. ST-REcN)). **g** Growth curves of fresh REcN,

S-REcN, SW-REcN, and W-REcN (REcN released from untreated WS/REcN), measured by OD600 over 12 h ($n = 3$ independent replicates, $P \leq 0.0001$ (S-REcN vs. REcN or SW-REcN or W-REcN)). **h** Fluorescence microscopy images of SW-REcN and S-REcN (Green: SYTO-9, Red: RFP, Scale bar: 100 μm). **i** Schematic of in vitro antimicrobial activity of REcN and SW-REcN against *Shigella flexneri* (*S. flexneri*), with pathogen reduction quantified by plating on MacConkey agar ($n = 5$ independent replicates, $P = 0.364$ (SW-REcN vs. REcN)). **j** In vivo probiotic resistance studies: orally administered REcN or WS/REcN with equivalent bacterial loads, with gastrointestinal tract imaging at 4 and 24 h post-administration ($n = 5$ biological independent replicates). All data are mean values ± standard deviations. Statistical analysis: One-way ANOVA with Tukey's multiple comparisons in (**e**–**g**) and Two-tailed unpaired *t*-test in (**i**) (*****P \leq 0.0001$, NS: not significant). **i**, **j** Created with BioRender.com released under a Creative Commons Attribution-NonCommercial-NoDerivs 4.0 International license.

pronounced sheet structures observed in the presence of the micro-organisms (Fig. 5c). In addition, WS/REcN was then obtained through thermal molding of water-plasticized silk/REcN powder at 60 °C. As shown in the SEM images, REcNs were randomly distributed and encapsulated within the silk with a granular structure (Fig. 5d left). Individual REcN with intact rod-like structures were surrounded by the granular silk matrix, as evidenced by the high-magnification SEM images (Fig. 5d right).

FTIR and XRD results identified β-sheet structural transformations in WS/REcN, indicating a high crystallinity transition in silk during the fabrication of silk-based living plastics (Supplementary Fig. 21). The release kinetics of REcN from silk matrices were monitored over 14 days, revealing that WS/REcN exhibited a sustained release profile, while TS/REcN (molded silk/REcN powder without plasticization) and silk/REcN showed faster release rates due to their lower crystallinity. The majority of REcN was released within the first 7 days for WS/REcN, demonstrating a more controlled, gradual release over the entire 14-day period. The cumulative release profiles suggest that WS/REcN serve as a promising candidate as a protective matrix for REcN (Supplementary Fig. 22). The viability of REcN released from silk/REcN, TS/REcN, and WS/REcN was also assessed, with over 72.7% of viable REcN retained in WS/REcN samples. There was no significant loss in bacterial viability across all processing steps, indicating that the plasticizer-assisted thermal molding process had minimal impact on the survival of the encapsulated REcN (Fig. 5e).

The in vitro assessment of REcN viability was further conducted using acidic simulated gastric fluid (SGF, pH 1.2), which is a primary barrier to effective probiotic oral administration[55,56]. After 2 h of incubation in SGF, the treated REcN samples were transferred to simulated intestinal fluid (SIF, pH 6.8) for an additional 2 h incubation to simulate the gastrointestinal transit (referred to as SGF + SIF treatment). Untreated REcN served as the control. The survival rates and fluorescence intensities of naked REcN significantly decreased following SGF and SGF + SIF treatments compared to the control, indicating damage and lethality of REcN due to the acidic environment (Supplementary Fig. 23). However, REcN exposed only to SIF showed no significant viability loss, demonstrating its resilience in simulated intestinal conditions.

The resistance of silk-based plastics to the gastrointestinal tract environment was evaluated by assessing the viability of encapsulated REcN following SGF + SIF treatments. SW-REcN (REcN released from treated WS/REcN) exhibited significantly higher viability than S-REcN (treated REcN) and ST-REcN (REcN released from treated TS/REcN) (Fig. 5f). After 12 h of incubation, OD600 growth curves showed that SW-REcN had growth rates comparable to W-REcN (REcN released from untreated WS/REcN) and fresh REcN, with significantly higher bacterial counts than S-REcN, in which almost no viable cells were detected (Fig. 5g). Fluorescence microscopy further confirmed that the majority of W-REcN and SW-REcN cells remained viable and comparable to fresh REcN, while fewer viable cells were observed in S-REcN (Fig. 5h and Supplementary Fig. 24). To assess the functionality of SW-REcN, an in vitro study was conducted using *Shigella flexneri* (*S. flexneri*) as a model pathogen, which is known to be inhibited by probiotics (Fig. 5i, Supplementary Fig. 25a)[33]. SW-REcN significantly reduced the pathogen load, with inhibition levels comparable to fresh REcN (Fig. 5i, Supplementary Fig. 25b), indicating that the functionality of REcN was preserved.

The in vivo gastrointestinal tolerance and retention of WS/REcN were evaluated in a murine model. Mice were orally administered either naked REcN suspension or WS/REcN, each containing 1×10^9 colony-forming units (CFU) of REcN. Biodistribution of REcN was monitored via fluorescence imaging at 4 and 24 h post-administration (Fig. 5j). At 4 h, both groups showed REcN in the stomach, but the WS/REcN group had significantly stronger fluorescence signals. By 24 h, only the WS/REcN group showed persistent signals throughout the

gastrointestinal tract, particularly in areas where probiotics typically colonize. Quantitative analyses confirmed that REcN level in the WS/REcN group remained significantly higher than in the naked REcN group at both time points (Supplementary Fig. 26). No fluorescence signals were detected in untreated mice or those fed with unlabeled WS/60 °C (Supplementary Fig. 27).

To further track the retention of the silk matrix, Cy7-labeled silk was synthesized and administered via oral gavage (Supplementary Fig. 28). Fluorescence imaging at 4 and 24 h revealed that while the Cy7 signal from Cy7-labeled WS/60 °C (Cy7-WS) and Cy7-labeled WS/REcN (Cy7-WS/REcN) diminished after 24 h, the RFP signal from REcN in Cy7-WS/REcN remained visible after 24 h, indicating that probiotics persisted in the gastrointestinal tract longer than the silk matrix (Supplementary Fig. 29). Notably, neither the silk matrix nor the probiotics distributed to major organs (heart, liver, spleen, kidneys, and lungs), demonstrating that they remained confined to the gastrointestinal tract post-administration. REcN viability was further confirmed through CFU analysis of intestinal tissues, showing significantly higher survival rates in the WS/REcN group compared to the naked REcN group at 24 h (Supplementary Fig. 30).

Additionally, primary blood biochemical indices and histological assessments of gastrointestinal tract tissues and major organs showed minimal changes after oral administration of WS/REcN and WS/60 °C (Supplementary Figs. 31–33), confirming the biosafety of this approach, with no signs of hematotoxicity or tissue damage. Collectively, these in vitro and in vivo results demonstrate that the highly crystalline silk matrix effectively protects and delivers live probiotics through the harsh conditions of the gastrointestinal tract.

As an alternative demonstration of utility for living silk plastics, the circular lifecycle of silk plastics was investigated. Previous studies have shown that protease XIV, proteinase K, and papain are proteases that degrade silk, with the biodegradability of silk challenged by the compact crystalline structure[32]. To explore low-cost, efficient methods for silk degradation while leveraging silk as a bioresource, we embedded rhizobacteria into the silk matrix to create a living material system (Fig. 6a). Nitrogen-fixing rhizobacteria strains are widely used as biofertilizers to enhance the yield of leguminous crops and reduce the dependency on expensive chemical nitrogen fertilizers[33,57,58]. Active rhizobacteria have been shown to secrete proteases and induce local pH acidification in moist soil, facilitating the degradation of organic materials. In this study, *Rhizobium tropici* CIAT 899 (CIAT 899) was selected as the model bacterium, incorporated into silk plastics using a plasticization process, and evaluated for its degradation potential in soil. SEM images showed that CIAT 899 was encapsulated within silk sheets prior to the molding process, exhibiting a morphology similar to that of the lyophilized silk/REcN powder (Fig. 6b). The structure of WS/CIAT 899 was observed after plasticizer-assisted thermal molding, where the sheet-like silk structure transformed into a granular morphology, accompanied by increased crystallinity in the silk matrix, resulting in the dense encapsulation of CIAT 899, as confirmed by FTIR and XRD analyses (Fig. 6c and Supplementary Fig. 34).

The sustained secretion of proteases by CIAT 899 cultured in bacterial media confirmed its viability within WS/CIAT 899, while WS/60 °C showed negligible protease activity (Supplementary Fig. 35). Degradation of WS/CIAT 899 was assessed over 90 days in soil (Fig. 6d). Optical microscopy, SEM, and digital images revealed that WS/CIAT 899 degraded from a rigid plastic to a sludge-like residue, while WS/60 °C remained mostly intact, with only minor surface erosion. SEM images further confirmed structural loosening and reduced thickness in WS/CIAT 899 compared to WS/60 °C (Fig. 6e), suggesting that both endogenous bacteria and external soil microorganisms contributed to silk protein degradation in WS/CIAT 899. A degradation assessment of WS/60 °C in protease XIV solution showed an average residual weight of 29.6% after 90 days. In soil, only 9.2% of WS/CIAT 899 remained undegraded, compared to the highly crystalline WS/60 °C, which
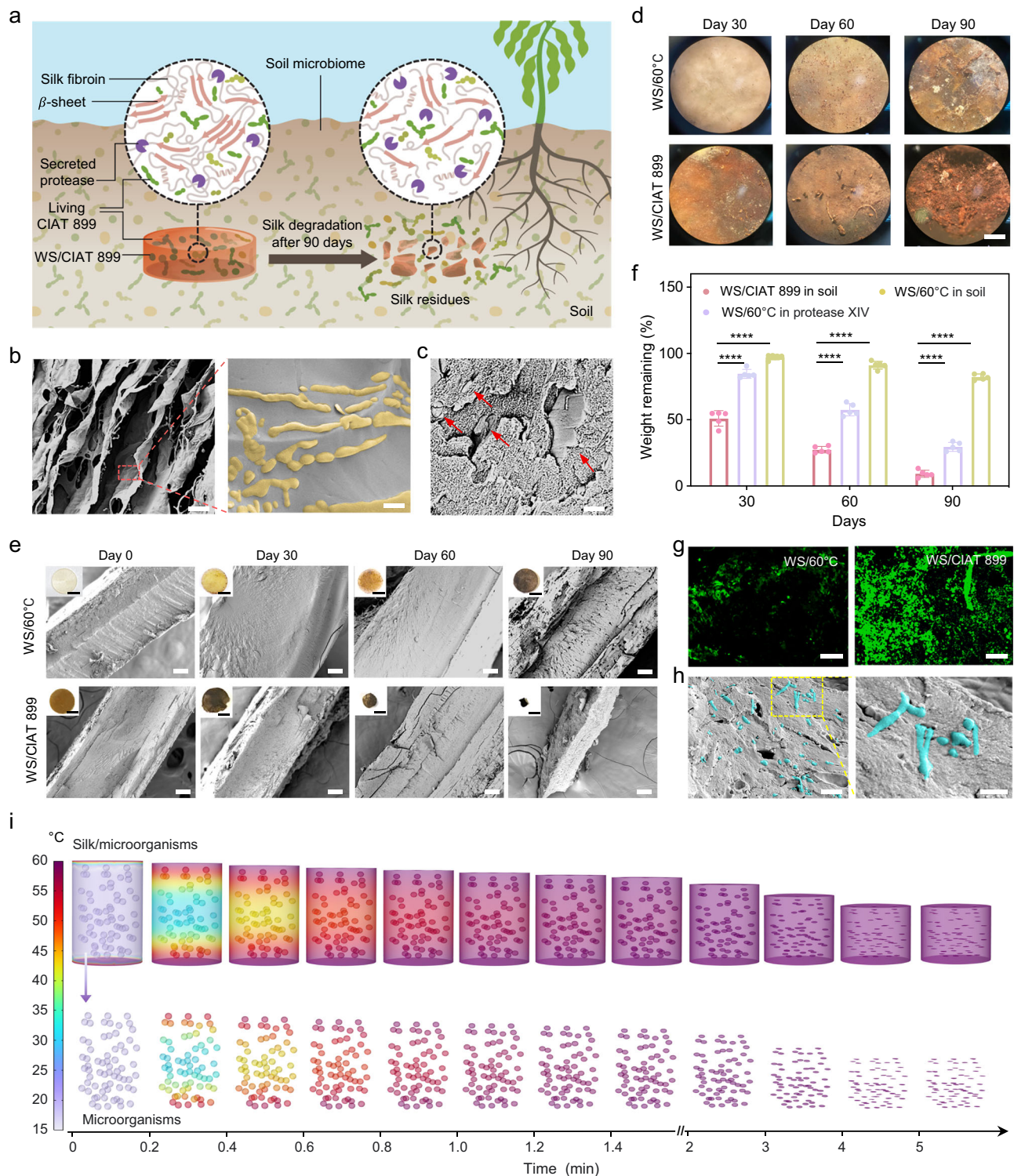
Fig. 6 | Degradation of WS/CIAT 899 silk-based living plastics in soil.
a Conceptual schematic illustrating the degradation of silk plastic by endogenous *Rhizobium tropici* CIAT 899 (CIAT 899) within a soil microbial community. **b** SEM images of silk/CIAT 899 powders (left) with magnified image (right) (Scale bars: 10 μm left, 500 nm right). **c** SEM image of WS/CIAT 899, with red arrows indicating the position of CIAT 899 (Scale bar: 1 μm). **d** Optical microscopy images of WS/60 °C and WS/CIAT 899 showing 90 day soil degradation profiles (Scale bar: 1 mm). **e** Cross-sectional SEM images of WS/60 °C and WS/CIAT 899 at days 0, 30, 60, and 90 (Scale bars: 100 μm). Insets are photographs corresponding to each SEM image (Scale bars: 5 mm). **f** Degradation profiles of WS/60 °C in soil and protease XIV, compared to WS/CIAT 899 in soil ($n = 5$ independent replicates, $P \le 0.0001$ (WS/CIAT 899 in soil vs. WS/60 °C in protease XIV at day 30), $P \le 0.0001$ (WS/CIAT 899

in soil vs. WS/60 °C in soil at day 30), $P \le 0.0001$ (WS/CIAT 899 in soil vs. WS/60 °C in protease XIV at day 60), $P \le 0.0001$ (WS/CIAT 899 in soil vs. WS/60 °C in soil at day 60), $P \le 0.0001$ (WS/CIAT 899 in soil vs. WS/60 °C in protease XIV at day 90), $P \le 0.0001$ (WS/CIAT 899 in soil vs. WS/60 °C in soil at day 90)). **g** Fluorescence microscopy images of WS/60 °C and WS/CIAT 899 at day 90 during soil degradation (Green: SYTO-9; Scale bar: 100 μm). **h** SEM image and magnified view of WS/CIAT 899 at day 90 during soil degradation (Scale bars: 1 μm left and 500 nm right). **i** FEA results showing stress and temperature distribution in the silk/microorganisms living system during thermal molding. Data shown as mean values ± standard deviations. Statistical analysis: Two-way ANOVA with Tukey's multiple comparisons in (**f**) (****$P \le 0.0001$).

retained 82.3% of its initial weight after 90 days. This observation indicated that WS/CIAT 899 underwent more efficient soil degradation (Fig. 6f). Fluorescence microscopy and SEM images confirmed the persistence and colonization of CIAT 899 within the silk plastic after 90 days of soil incubation (Fig. 6g, h). These results indicate that silk-based living plastics support sustained microbial retention for the degradation of the silk matrix in soil.

Finite element analysis (FEA) was performed to model temperature and stress distributions during the plasticizer-assisted thermal molding process. Results showed that Von Mises stress peaked at 4 min, with higher stress on the outer silk surfaces compared to internal microorganisms (Supplementary Fig. 36a, b). The WS/microorganisms reached 60 °C within 1 min, achieving uniform heat distribution, aligning with experimental data (Fig. 6i and Supplementary Fig. 36c). These findings offer valuable guidance for scaling up silk-based living material systems with diverse biotic components.

In summary, this study introduces silk plastics as a platform for living material systems, utilizing a mild plasticizer-assisted thermal molding technique that lowers processing temperatures to preserve bacterial viability and functionality. The use of plasticizers facilitated the transition of silk to a highly crystalline structure at 60 °C, creating robust silk plastics suitable for microbial incorporation in both aqueous and soil environments. Enhanced survival of probiotic REcN in silk plastics was confirmed through in vitro simulated gastrointestinal fluid treatments and in vivo oral administration models. Additionally, the plastics degraded within 90 days in soil, facilitated by the nitrogen-fixing bacterium CIAT 899, underscoring the long-term functionality of microorganisms in degradable silk-based materials. Overall, these findings suggest that silk-based living materials with dense structures can effectively preserve bioactive, living components. This eco-friendly approach provides a sustainable pathway for developing living material systems with potential applications in degradable polymers, medicine, environmental sustainability, and agriculture.

Methods

Ethical approval statement
All animal experiments were conducted in accordance with guidelines and approved by the Institutional Animal Care and Use Committee of Tufts University Medical Center (animal protocol M2022-121 and M2023-113). All mice (5 mice per cage) were housed in a specific pathogen-free environment at a temperature of 18–22 °C and a humidity of 50–60%. All mice were promptly euthanized using CO_2 gas after finishing animal experiment.

Sex of the animal models
The intestinal structure and inflammatory responses in subcutaneous encapsulation do not have sex-specific variability based on current scientific understanding. Therefore, in this work, the biological properties of the compounds were studied only in male mice for consistency.

Silk fibroin plasticization and thermal molding
A regenerated *Bombyx mori* silk solution was prepared as follows. *Bombyx mori* silkworm cocoons were cut into small pieces and boiled in a 0.02 M Na_2CO_3 solution for 30 min to remove the sericin layer. The degummed silk was then dried and dissolved in a 9.3 M lithium bromide (LiBr, Sigma-Aldrich, USA) solution at 60 °C for 4 h, followed by dialysis (MWCO 3500, Spectrum, USA) for 72 h to completely remove LiBr. The resulting silk solution was centrifuged for 20 min at 10,414 g twice. The silk solution was diluted (~1% w/v), frozen using liquid nitrogen, and lyophilized at −80 °C and 0.006 bar until complete sublimation. The lyophilized silk was milled into amorphous silk powder using a high-speed analytical mill. This powder was plasticized at 4 °C with mist treatment from a humidifier to achieve the desired water content before further processing. Plasticized silk powders were

packed into predesigned molds and subjected to thermal pressing at 632 MPa at various temperatures for 15 min.

^{13}C Solid-state nuclear magnetic resonance (^{13}C SSNMR)
^{13}C SSNMR experiments were performed using a Bruker AVANCE III HD 600 MHz spectrometer (Bruker BioSpin GmBH, Germany), with ^{13}C and ^{1}H resonance frequencies of 150.90 and 600.13 MHz, respectively. All experiments were conducted in a 4 mm CP/MAS broadband probe. A pulse sequence with a ramped (100-50) ^{1}H − ^{13}C cross-polarization (CP) period followed by ^{1}H-decoupled ^{13}C detection was used. The contact time and ^{1}H decoupling field strength were 1 ms and 69 kHz, respectively. The recycle delay was 3–4 s. All the experiments were conducted at ambient temperature. The magic angle spinning speed was 8 kHz for all samples. The chemical shift was calibrated using 1,4-di-tert-butylbenzene by setting the unprotonated carbon signal to 148.8 ppm. Deconvolution of ^{13}C SSNMR spectra was performed using OriginLab software (OriginLab, 2024, USA), with a Gaussian function selected to fit the regions corresponding to Ala, Gly, and Ser residues (12–70 ppm and 165–180 ppm). Fitted peak centers, peak areas, and full-width-at-half-maximum were calculated for structural determination.

Preparation of silk living materials
The non-pathogenic *Escherichia coli* Nissle 1917 (ECN) strain was generously provided by Prof. Christopher A. Voigt lab. The pDawn plasmid, originally a gift from Andreas Moeglich (Addgene #43796), was modified to include the red fluorescence protein (RFP) gene, which was amplified via PCR using primers 5′-GTA GTA CAT ATG GCC TCC TCC GAG GAC-3′ and 5′-GAT GAT CTC GAG TTA GGC GCC GGT GGA GTG-3′ (Millipore Sigma, USA). The RFP gene and the pDawn plasmid were digested with NdeI and XhoI restriction enzymes (Thermo Fisher, USA) and ligated using standard, commercially established molecular biology techniques to create the pDawn-RFP reporter plasmid.

Transformed colonies were selected on Luria-Bertani (LB) agar (Fisher Scientific, USA) containing 50 µg/mL kanamycin (Kan). The EcN strain with pDawn-RFP (REcN) was initially inoculated in 5 mL of LB medium with 50 µg/mL Kan and cultured at 37 °C with shaking at 250 rpm for 18 h. REcN harbors the gene cassette for RFP expression, with the plasmid maintained by a kanamycin resistance marker.

The REcN culture was then used to inoculate in a larger flask containing the desired volume of culture medium, grown to an OD600 of 1 under the same conditions. Cell pellets were collected by centrifuging 30 mL of REcN culture at OD600 of 1 at 1575 g for 10 min, and the supernatant was discarded. The bacterial pellet was washed with PBS and subsequently mixed with pre-prepared silk solutions. Finally, 30 mL of 1% w/v silk solution was thoroughly mixed with the centrifuged REcN cell pellets, frozen, and lyophilized at −80 °C and 0.006 bar.

Rhizobium tropici strain CIAT 899 (CIAT 899, ATCC 49672, USA) was routinely cultured on rhizobium X agar at 30 °C in a static incubator or in rhizobium X broth in 14 mL culture tubes, shaken at 250 rpm at 30 °C in a shaker incubator until an OD600 of 1 was reached. Following a similar preparation to the REcN silk composites described above, 30 mL of 1% w/v silk solution was mixed with cell pellets obtained by centrifuging 30 mL of CIAT 899 culture (OD600 = 1) at 10,414 g for 20 min. The resulting CIAT 899 and silk mixture was then freeze-dried at −80 °C and 0.006 bar.

TS/REcN samples were prepared by direct thermal molding of silk/REcN powders at 632 MPa and 60 °C for 15 min. WS/REcN and WS/CIAT 899 samples were prepared by thermal molding plasticized silk/REcN or silk/CIAT 899 powders using a procedure similar to the preparation of plasticized silk powders, at 60 °C for 15 min.

Molecular dynamics simulation
The initial silk protein structure was modeled based on the theoretically predicted structure in the Protein Data Bank (PDB ID: 2SLK). The

silk protein sequence (amino acids 152-586, UniProt ID: P05790) was selected for these simulations. A 200 ns conventional molecular dynamics (MD) simulation was performed under the Generalized Born implicit solvent model, with a Born radius of 12 Å and an ion concentration of 0.05 M. The CHARMM36m force field parameters were used[59], and the temperature was maintained at 25 °C using a Langevin thermostat[60]. The SHAKE algorithm was applied to constrain bond lengths involving hydrogen atoms, with an integration step of 2 fs. After equilibration, the equilibrated structure was used for further MD simulations.

Two types of silk protein models were constructed: one anhydrous and the other containing 452 TIP3P water molecules (20% water mass)[61]. Before MD simulations, 50,000 steps of conjugation gradient minimization were performed to release some high-energy contact in the protein structures. After that, the equilibrium MD simulations of 200 ns were carried out to obtain stable structures under the isothermal-isobaric ensemble. The simulation temperature in the stage was kept at 25 °C by a Langevin thermostat, and the pressure of the systems was adjusted to 1 atm by the modified Nosé-Hoover Langevin piston method[62]. Simulations at 4 °C and 60 °C with a pressure of 625 MPa were conducted to mimic experimental conditions. All MD simulations were performed using NAMD 2.14[63] with periodic boundary conditions, and nonbonded interactions were truncated between 10–12 Å. The PME method was used for electrostatic interactions, and visualization of simulation trajectories was done with VMD and PyMOL[64]. Protein conformations were analyzed using the STRIDE method[65].

Characterization of silk-based materials

The morphologies of silk powder, 20% WSP, WS/60 °C, and micropillars were characterized using field-emission scanning electron microscopy (SEM) (Gemini 560, ZEISS, Germany). SEM images were collected at 5 kV, with samples prepared by sputtering a 20 nm layer of Pt/Pd. Cross-sectional morphologies of lyophilized silk samples containing encapsulated microorganisms were imaged under the same conditions.

Thermal properties were analyzed using differential scanning calorimetry (DSC, Q20, TA Instruments, USA) and thermogravimetric analysis (TGA, Q50, TA Instruments, USA). For each test, samples (3–5 mg) were placed in an aluminum pan under nitrogen gas. TGA measurements were conducted from room temperature to 500 °C at a rate of 10 °C/min. DSC scans were performed from −50 to 200 °C at a rate of 10 °C/min under a dry nitrogen flow (50 mL/min).

X-ray diffraction (XRD) patterns of the samples were obtained using a Rigaku SmartLab system (Rigaku Corporation, Japan) with CuKα radiation ($\lambda = 1.5418$ Å) at room temperature. XRD measurements were conducted in a parallel beam setting within the 2θ range of 5–50 °, with a step size of 0.01 ° and a scanning speed of 2 °/min. The voltage and current were set to 45 kV and 200 mA, respectively.

Fourier transform infrared spectroscopy (FTIR) was performed on a JASCO FTIR 6200 spectrometer equipped with a MIRacle attenuated total reflectance (ATR) germanium crystal cell in absorbance mode. Each spectrum was recorded over 64 scans with a resolution of 4.0 cm⁻¹.

Tensile tests were conducted using a mechanical testing machine (5565, Instron, USA) in tensile mode at 25 °C, with a loading rate of 1 mm/min. Samples measuring 10 mm in length and 5 mm in width were tested in triplicate.

Finite element analysis

Finite element analysis (FEA) was conducted using the Structural Mechanics and MEMS modules in COMSOL Multiphysics 6.1 (COMSOL, Sweden). The model consisted of microorganism spheres, each with a diameter of 1 μm, randomly placed within a silk cylinder (3 mm height, 2 mm diameter) at a volume ratio of 1:9 (microorganism spheres to cylinder). Both the spheres and cylinder were modeled as linear elastic materials, with the Young's modulus obtained experimentally. Constraints were applied to simulate the molding process.

In the heat transfer field, the processing temperature was set to 60 °C. The solid mechanics field was coupled with the heat transfer field through the thermal expansion module. A free tetrahedral mesh with an average element size close to 1 was used for refined mesh division. For accurate time-step control, a time-dependent solver with backward differentiation formulation and a relative tolerance of 0.001 was applied.

Cell culture

C2C12 mouse skeletal myoblast cells (CRL-1772, ATCC, USA) were cultured in Dulbecco's eagle medium (DMEM, Gibco, USA) supplemented with 10% fetal bovine serum and 1% antibiotic-antimycotic (Gibco, USA) in standard culture conditions, 37 °C and 5% CO_2 humidified atmosphere. C2C12 cells were seeded onto each silk micropillar and incubated at 37 °C with 5% CO_2 for 1 h to allow adhesion (5×10^6 cells/each micropillar). Micropillars were then transferred to 24-well plates for further culture. Cell activity on each silk micropillar was assessed using the alamarBlue assay (Invitrogen, USA). Silk micropillars were incubated with alamarBlue reagent for 2 h, and fluorescence was measured using a microplate reader at 560/590 nm (Varioskan™ LUX multimode, ThermoFisher Scientific, USA). Immunofluorescence staining was performed by fixing cells with 4% paraformaldehyde and permeabilizing with 0.1% Triton X-100 (Invitrogen, USA). Cells were then blocked in 3% bovine serum albumin solution (BSA, Sigma-Aldrich, USA) for 30 min and incubated with myosin heavy chain antibody MF20 (2.5 μg/mL, Invitrogen, USA) in 0.3% BSA blocking solution at 4 °C overnight, followed by staining with Goat anti-Mouse Alexa Fluor™ 594 secondary antibody (1: 400, Invitrogen, USA), Alexa Fluor™ 488 Phalloidin (1:400, Invitrogen, USA), and 4′,6-diamidino-2-phenylindole (1: 500, DAPI, Invitrogen, USA) in 0.3% BSA blocking solution at room temperature for 1 h. Imaging was performed using a confocal laser scanning microscope (SP 8, Leica, Germany).

In vivo biocompatibility

All animal studies were reviewed and approved by the Institutional Animal Care and Use Committee of Tufts University Medical Center (animal protocol M2022-121). Before implantation, WS/60 °C and TS/60 °C were machined into a round shape with a diameter of 4 mm and a thickness of 0.6 mm. All samples were sterilized by ethylene oxide before the implantation. For the studies, 8 week-old male C57BL/6 mice (Charles River Laboratories, USA) were anesthetized with 5% isoflurane in oxygen for induction and 2.5% for maintenance. After creating a 1 cm incision, a blunt dissection was performed to insert the silk implant subcutaneously, and the incision was closed with skin clips. The animals were euthanized by CO_2 inhalation at the 7, 14, and 28 days post-implantation. The tissues were excised and collected for histological and immunofluorescence assessments. Tissue samples were fixed in 4% paraformaldehyde and dehydrated through a series of graded ethanol solutions and then embedded in paraffin. Sections of 5 μm thickness were cut using a microtome, followed by deparaffinization in xylene and rehydration in sequential ethanol and distilled water baths. Subsequently, the sections were stained with haematoxylin and eosin (H&E) and Masson's trichrome.

For immunofluorescence staining, the slides were deparaffinized with xylene and ethanol, followed by rehydration with deionized water. Antigen retrieval was performed in IHC-Tek epitope retrieval solution (IW-1100, IHC world LLC, USA) with the IHC-Tek epitope retrieval steamer (IHC world LLC, USA). Then the slides were incubated in primary antibodies (1: 200 mouse anti-α-SMA for myofibroblast (ab7817, Abcam, USA); 1: 200 rabbit anti-collagen-I for collagen (ab21286, Abcam, USA); 1: 200 mouse anti-CD68 for macrophages (ab201340, Abcam, USA)) diluted with IHC-Tek antibody diluent (IHC world LLC, USA) for 1 h at

room temperature. The slides were then stained with Alexa Fluor 488 labeled anti-rabbit (1: 200 goat anti-rabbit IgG (H + L) highly cross-adsorbed secondary antibody, Invitrogen, USA) or Alexa Fluor 488 labeled anti-mouse secondary antibodies (1: 200 goat anti-mouse IgG (H + L) cross-adsorbed secondary antibody, Invitrogen, USA) for 1 h at room temperature. All slides were counterstained with DAPI (ab104139, Abcam, USA) for 20 min. A fluorescence microscope (BZ-X700, Keyence, USA) was used for image acquisition. ImageJ was used to quantify the fluorescence intensity of expressed proteins.

Release kinetics of REcN from WS/REcN and TS/REcN

To evaluate the release kinetics of REcN from the silk matrix, silk/REcN powder, TS/REcN, and WS/REcN samples were incubated in 5 mL of PBS at 4 °C. At predetermined time points, aliquots of the bacterial suspension were withdrawn and replaced with fresh PBS to maintain consistent conditions. Fluorescence measurements (Ex/Em: 554/591 nm) were taken using a multimode microplate reader (Varioskan™ LUX, ThermoFisher Scientific, USA) to assess bacterial concentration. The percentage of released REcN was calculated by comparing the fluorescence values to those of a suspension containing an equivalent mass of naked REcN encapsulated in the silk matrix at each time point.

Viability test

Silk/REcN powder, TS/REcN, and WS/REcN samples were incubated in 5 mL of PBS for 24 h. Aliquots (100 μL) of serially diluted bacterial suspensions released from the silk/REcN powder, TS/REcN, and WS/REcN were plated on LB/Kan agar. After overnight incubation at 37 °C, the number of colonies was manually counted. The viability of REcN was calculated by dividing the colony-forming unit (CFU) counts from the plates by the corresponding CFU values obtained from fluorescence measurements after 12 h of release, as previously described.

Resistance assay and proliferation activity assessments in vitro

Simulated gastric fluid (SGF, 0.2% sodium chloride in 0.7% hydrochloric acid, pH 1.0-1.4, Ricca Chemical, USA) supplemented with 3.2 mg/mL of pepsin from porcine gastric mucosa (Sigma-Aldrich, USA) and simulated intestinal fluid (SIF, pancreatin, potassium dihydrogen phosphate, and sodium hydroxide, pH 6.7-6.9, Ricca Chemical, USA) were used to mimic the gastrointestinal tract environment. Naked REcN (5×10^8 CFUs) and lyophilized WS/REcN and TS/REcN (equivalent REcN load) were suspended in 5 mL of SGF and incubated in a 37 °C incubator at 250 rpm for 2 h. To better simulate gastrointestinal transit, the SGF treated samples were then transferred to 5 mL of SIF for an additional 2 h of incubation. Following these treatments, naked REcN and REcN released from WS/REcN and TS/REcN were collected and resuspended in PBS for viability assessments as described above. The untreated naked REcN and released REcN from untreated WS/REcN or TS/REcN served as control groups for their corresponding resistance assessments.

For proliferation activity assessments, the optical density at 600 nm (OD600) of the collected REcN from naked REcN and WS/REcN groups (both with and without the simulated gastrointestinal fluid treatment) was adjusted to 0.05 in LB/Kan medium. OD600 values were recorded at 30 min intervals using a microplate reader (Varioskan™ LUX multimode, ThermoFisher Scientific, USA) at 37 °C to generate growth curves over 12 h culture. Additionally, fluorescence measurements were performed using the microplate reader (Ex/Em: 554/591 nm) to monitor intensity changes of RFP-labeled REcN. Further analysis included live/dead bacterial staining (Invitrogen, USA), followed by imaging via fluorescence microscopy (BZ-X700, Keyence, USA).

In Vitro evaluation of WS/REcN against *Shigella flexneri*

Fresh REcN and SW-REcN (REcN released from SGF + SIF-treated WS/REcN) were collected to assess their antimicrobial activity against the gut pathogen *Shigella flexneri* (*S. flexneri*, 12022 GFP, ATCC, USA). The pathogen reduction efficacy was evaluated by co-incubating the REcN or SW-REcN with *S. flexneri* at a 1:1 CFU/mL ratio for 6 h at 37 °C. Following incubation, serial dilutions of the mixtures (100 μL) were plated onto MacConkey agar and incubated at 37 °C. Colony differentiation was based on lactose fermentation: *S. flexneri* (lactose-negative, Lac−) formed yellowish colonies, while REcN (lactose-positive, Lac +) produced pink colonies. Viable *S. flexneri* colonies were further confirmed by fluorescence imaging using a gel imager (ChemiDoc XRS + , ImageLab v.6.1, Bio-Rad), where GFP-positive S. flexneri emitted a red fluorescence signal. The pathogen reduction was calculated by dividing the remaining viable *S. flexneri* colonies by the total amount of *S. flexneri* before treatment.

Administration route investigation and biosafety assessment

All animal studies were reviewed and approved by the Institutional Animal Care and Use Committee of Tufts University Medical Center (animal protocol M2023-113). Sulfo-cyanine 7-NHS ester (Cy7, Lumiprobe, USA) was dissolved in water at a concentration of 0.5 % (w/v) and reacted with a silk solution for 24 h in the dark. The resulting mixture was dialyzed using a dialysis membrane (MWCO: 3.5 kDa, Spectrum, USA) to remove residual Cy7, yielding a Cy7-labeled silk solution. Cy7-WS and Cy7-WS/REcN samples were prepared following the WS/60 °C and WS/REcN procedure described above, using the Cy7-silk solution in place of the regular silk solution. Fluorescence imaging was conducted using an in vivo imaging system (Lago X, Spectral Instrument Imaging, USA). WS/60 °C, Cy7-WS, WS/REcN, and Cy7-WS/REcN samples were imaged under both the RFP channel (Ex/Em: 570/610 nm) and Cy7 channel (Ex/ Em: 745/790 nm), respectively.

For ex vivo imaging, 8 week-old male C57BL/6 mice (Charles River Laboratories, USA) were fed an irradiated AIN-93M imaging diet (BioServe, USA) for at least 1 week before experiments to reduce background fluorescence. Mice were fasted overnight before being administered WS/60 °C, Cy7-WS, naked REcN (1×10^9 CFUs), WS/REcN, and Cy7-WS/REcN (containing equivalent CFUs of REcN). At designated time points, the mice were euthanized, and their organs (heart, liver, spleen, lungs, kidneys, and gastrointestinal tract) were harvested, rinsed with PBS, and imaged using both the RFP and Cy7 channels. The total radiant efficiency was quantified using Aura software (Spectral Instrument Imaging, USA). To assess the retention and bioavailability of REcN, large intestine tissues (cecum and colon) were homogenized in PBS and the suspensions (100 μL) were plated in sequential dilutions for living colony counts using the LB/Kan agar plate. To access the oral biosafety, male BALB/c mice (6–8 weeks, Charles River Laboratories, USA) were euthanized at 24 h after oral administration of PBS, 20 mg of WS/60 °C, and 20 mg of WS/REcN (REcN: 10^9 CFUs), respectively. After treatment, aliquots of blood were collected for blood routine and blood chemistry analysis. The tissues of mice, including the gastrointestinal tract and major organs (heart, lungs, liver, kidneys, and spleen) were excised and stained with H&E (Leica Biosystems, Germany) for histopathological evaluation, followed by imaging using a Hamamatsu Nanozoomer 2.0-HT slide scanning system.

Protease secretion and degradation measurements

WS/60 °C and WS/CIAT 899 were incubated in rhizobium X medium, and protease secretion in the supernatant was measured using a protease activity assay kit (Abcam, USA). For degradation in soil, WS/60 °C and WS/CIAT 899 were loaded in nylon mesh bags with a pore size of 100 μm under standard environmental conditions and then placed in soil with a moisture content of 25% for a degradation period of 90 days. Samples were cleaned, dried, and weighed at regular intervals to assess degradation. WS/60 °C samples were also incubated in 1 U/mL protease XIV (Sigma-Aldrich, USA) at 37 °C for degradation studies. After rinsing with deionized water and drying, the remaining mass of the sample after incubation was recorded for degradation analysis.

Statistics and reproducibility

GraphPad Prism 9 was used for all statistical analyses and all data are shown as means ± standard deviations. In the statistical analysis for comparison between multiple samples, One-way or two-way analysis of variance (ANOVA) followed by Tukey's multiple comparison tests was conducted. For the statistical analysis between two data groups, the Two-tailed unpaired t-test was conducted. Significance thresholds were *$P \leq 0.05$, **$P \leq 0.01$, ***$P \leq 0.001$, ****$P \leq 0.0001$, and NS, not significant. The number of replicates performed is detailed in each figure legend, where applicable. For the data in Fig. 3b, d; 4b; 5c, d, h; 6b–e, g, h and Supplementary Figs. 17b; 24, three independent experiments were repeated independently with similar results and results from representative experiments were shown.

Reporting summary

Further information on research design is available in the Nature Portfolio Reporting Summary linked to this article.

Data availability

The data that support the findings of this study are available within this article and its Supplementary Information. Data is also available from the corresponding author upon request. Source data are provided with this paper.

References

1. Fraser, C. M., Eisen, J. A. & Salzberg, S. L. Microbial genome sequencing. *Nature* **406**, 799–803 (2000).
2. Schmitz, A. M. et al. Generation of a Gluconobacter oxydans knockout collection for improved extraction of rare earth elements. *Nat. Commun.* **12**, 6693 (2021).
3. Cotruvo, J. A. Jr, Featherston, E. R., Mattocks, J. A., Ho, J. V. & Laremore, T. N. Lanmodulin: a highly selective lanthanide-binding protein from a lanthanide-utilizing bacterium. *J. Am. Chem. Soc.* **140**, 15056–15061 (2018).
4. Tang, C. et al. Degradable living plastics programmed by engineered spores. *Nat. Chem. Biol.* https://doi.org/10.1038/s41589-024-01713-2 (2024).
5. Kim, H. et al. Biocomposite thermoplastic polyurethanes containing evolved bacterial spores as living fillers to facilitate polymer disintegration. *Nat. Commun.* **15**, 3338 (2024).
6. Tang, T. C. et al. Materials design by synthetic biology. *Nat. Rev. Mater.* **6**, 332–350 (2021).
7. Mimee, M. et al. An ingestible bacterial-electronic system to monitor gastrointestinal health. *Science* **360**, 915–918 (2018).
8. Ostrov, N. et al. A modular yeast biosensor for low-cost point-of-care pathogen detection. *Sci. Adv.* **3**, e1603221 (2017).
9. Wang, Q., Hu, Z., Li, Z., Liu, T. & Bian, G. Exploring the application and prospects of synthetic biology in engineered living materials. *Adv. Mater.* **7**, 2305828 (2023).
10. An, B. et al. Engineered living materials for sustainability. *Chem. Rev.* **123**, 2349–2419 (2022).
11. Sandak, A. Engineered living materials for sustainable and resilient architecture. *Nat. Rev. Mater.* **8**, 1–3 (2023).
12. McBee, R. M. et al. Engineering living and regenerative fungal–bacterial biocomposite structures. *Nat. Mater.* **21**, 471–478 (2022).
13. González, L. M., Mukhitov, N. & Voigt, C. A. Resilient living materials built by printing bacterial spores. *Nat. Chem. Biol.* **16**, 126–133 (2020).
14. Rodrigo-Navarro, A., Sankaran, S., Dalby, M. J., del Campo, A. & Salmeron-Sanchez, M. Engineered living biomaterials. *Nat. Rev. Mater.* **6**, 1175–1190 (2021).
15. Heveran, C. M. et al. Biomineralization and successive regeneration of engineered living building materials. *Matter* **2**, 481–494 (2020).
16. Chen, B. et al. Programmable living assembly of materials by bacterial adhesion. *Nat. Chem. Biol.* **18**, 289–294 (2022).
17. Peng, R. et al. Embedding living cells with a mechanically reinforced and functionally programmable hydrogel fiber platform. *Adv. Mater.* **35**, 2305583 (2023).
18. Duraj-Thatte, A. M. et al. Genetically programmable self-regenerating bacterial hydrogels. *Adv. Mater.* **31**, 1901826 (2019).
19. Sankaran, S. & Del Campo, A. Optoregulated protein release from an engineered living material. *Adv. Biosyst.* **3**, 1800312 (2019).
20. Zhao, S., Guo, C., Kumarasena, A., Omenetto, F. G. & Kaplan, D. L. 3D printing of functional microalgal silk structures for environmental applications. *ACS Biomater. Sci. Eng.* **5**, 4808–4816 (2019).
21. Vepari, C. & Kaplan, D. L. Silk as a biomaterial. *Prog. Polym. Sci.* **32**, 991–1007 (2007).
22. Sahoo, J. K., Hasturk, O., Falcucci, T. & Kaplan, D. L. Silk chemistry and biomedical material designs. *Nat. Rev. Chem.* **7**, 1–17 (2023).
23. Huang, W., Ling, S., Li, C., Omenetto, F. G. & Kaplan, D. L. Silkworm silk-based materials and devices generated using bio-nanotechnology. *Chem. Soc. Rev.* **47**, 6486–6504 (2018).
24. Li, C. et al. Design of biodegradable, implantable devices towards clinical translation. *Nat. Rev. Mater.* **5**, 61–81 (2020).
25. Ling, S., Kaplan, D. L. & Buehler, M. J. Nanofibrils in nature and materials engineering. *Nat. Rev. Mater.* **3**, 1–15 (2018).
26. Miao, B. et al. An interfacial-assembled self-supporting nanofilm induced by strong intermolecular interaction between silk fibroin and lysozyme. *Adv. Funct. Mater.* **34**, 2312324 (2024).
27. Hasturk, O., Sahoo, J. K. & Kaplan, D. L. Synthesis and characterization of silk-poly (guluronate) hybrid polymers for the fabrication of dual crosslinked, mechanically dynamic hydrogels. *Polymer* **281**, 126129 (2023).
28. Wang, Y. et al. Silk-protein-based gradient hydrogels with multimode reprogrammable shape changes for biointegrated devices. *Proc. Natl. Acad. Sci. USA* **120**, e2305704120 (2023).
29. Choi, J. et al. Instantaneous formation of silk protein aerosols and fibers with a portable spray device under ambient conditions. *Adv. Mater. Technol.* **8**, 2201392 (2023).
30. Tsioris, K. et al. Fabrication of silk microneedles for controlled-release drug delivery. *Adv. Funct. Mater.* **22**, 330–335 (2012).
31. Tran, H. A. et al. Emerging silk fibroin materials and their applications: New functionality arising from innovations in silk crosslinking. *Mater. Today* **65**, 244–259 (2023).
32. Guo, C. et al. Thermoplastic moulding of regenerated silk. *Nat. Mater.* **19**, 102–108 (2020).
33. Jimenez, M. et al. Synthetic extremophiles via species-specific formulations improve microbial therapeutics. *Nat. Mater.* **23**, 1436–1443 (2024).
34. Chen, Y. et al. Reinforcement of the intestinal mucosal barrier via mucus-penetrating PEGylated bacteria. *Nat. Biomed. Eng.* **8**, 823–841 (2024).
35. Hou, W. et al. Decorating bacteria with a therapeutic nanocoating for synergistically enhanced biotherapy. *Small* **17**, 172101810 (2021).
36. Rosenboom, J.-G., Langer, R. & Traverso, G. Bioplastics for a circular economy. *Nat. Rev. Mater.* **7**, 117–137 (2022).
37. DelRe, C. et al. Near-complete depolymerization of polyesters with nano-dispersed enzymes. *Nature* **592**, 558–563 (2021).
38. Yoshida, S. et al. A bacterium that degrades and assimilates poly (ethylene terephthalate). *Science* **351**, 1196–1199 (2016).
39. Yazawa, K., Ishida, K., Masunaga, H., Hikima, T. & Numata, K. Influence of water content on the β-sheet formation, thermal stability, water removal, and mechanical properties of silk materials. *Biomacromolecules* **17**, 1057–1066 (2016).
40. Asakura, T., Endo, M., Tasei, Y., Ohkubo, T. & Hiraoki, T. Hydration of Bombyx mori silk cocoon, silk sericin and silk fibroin and their interactions with water as studied by 13 C NMR and 2 H NMR relaxation. *J. Mater. Chem. B* **5**, 1624–1632 (2017).
41. Callone, E., Dirè, S., Hu, X. & Motta, A. Processing influence on molecular assembling and structural conformations in silk fibroin:

elucidation by solid-state NMR. *ACS Biomater. Sci. Eng.* **2**, 758–767 (2016).

42. Stengel, D. et al. Hydration-induced β-sheet crosslinking of α-helical-rich spider prey-wrapping silk. *Adv. Funct. Mater.* **31**, 2007161 (2021).

43. Nishimura, A., Matsuda, H., Tasei, Y. & Asakura, T. Effect of water on the structure and dynamics of regenerated [3-13C] Ser,[3-13C], and [3-13C] Ala-Bombyx mori silk fibroin studied with 13C solid-state nuclear magnetic resonance. *Biomacromolecules* **19**, 563–575 (2018).

44. Yoshimizu, H. & Asakura, T. The structure of Bombyx mori silk fibroin membrane swollen by water studied with ESR, 13C-NMR, and FT-IR spectroscopies. *J. Appl. Polym. Sci.* **40**, 1745–1756 (1990).

45. Hu, X., Kaplan, D. & Cebe, P. Determining beta-sheet crystallinity in fibrous proteins by thermal analysis and infrared spectroscopy. *Macromolecules* **39**, 6161–6170 (2006).

46. Hu, X., Kaplan, D. & Cebe, P. Effect of water on the thermal properties of silk fibroin. *Thermochim. Acta* **461**, 137–144 (2007).

47. Tamada, Y. New process to form a silk fibroin porous 3-D structure. *Biomacromolecules* **6**, 3100–3106 (2005).

48. Zhang, D. et al. Dealing with the foreign-body response to implanted biomaterials: strategies and applications of new materials. *Adv. Funct. Mater.* **31**, 2007226 (2021).

49. Cramer, M. et al. Tissue response, macrophage phenotype, and intrinsic calcification induced by cardiovascular biomaterials: can clinical regenerative potential be predicted in a rat subcutaneous implant model? *J. Biomed. Mater. Res. A* **110**, 245–256 (2022).

50. Noskovicova, N. et al. Suppression of the fibrotic encapsulation of silicone implants by inhibiting the mechanical activation of pro-fibrotic TGF-β. *Nat. Biomed. Eng.* **5**, 1437–1456 (2021).

51. Deng, J. et al. Electrical bioadhesive interface for bioelectronics. *Nat. Mater.* **20**, 229–236 (2021).

52. Zhang, X., Chen, G., Zhang, H., Shang, L. & Zhao, Y. Bioinspired oral delivery devices. *Nat. Rev. Bioeng.* **1**, 208–225 (2023).

53. Zhang, F. et al. Gastrointestinal tract drug delivery using algae motors embedded in a degradable capsule. *Sci. Robot.* **7**, eabo4160 (2022).

54. Schultz, M. Clinical use of E. coli Nissle 1917 in inflammatory bowel disease. *Inflamm. Bowel Dis.* **14**, 1012–1018 (2008).

55. Yang, X. et al. Physiologically inspired mucin coated Escherichia coli Nissle 1917 enhances biotherapy by regulating the pathological microenvironment to improve intestinal colonization. *ACS Nano* **16**, 4041–4058 (2022).

56. Zhang, C. et al. Bacteria-induced colloidal encapsulation for probiotic oral delivery. *ACS Nano* **17**, 6886–6898 (2023).

57. Zvinavashe, A. T. et al. Degradation of regenerated silk fibroin in soil and marine environments. *ACS Sustain. Chem. Eng.* **10**, 11088–11097 (2022).

58. Zvinavashe, A. T. et al. Programmable design of seed coating function induces water-stress tolerance in semi-arid regions. *Nat. Food* **2**, 485–493 (2021).

59. Huang, J. et al. CHARMM36m: an improved force field for folded and intrinsically disordered proteins. *Nat. Methods* **14**, 71–73 (2017).

60. Hoover, W. G. Canonical dynamics: equilibrium phase-space distributions. *Phys. Rev. A* **31**, 1695 (1985).

61. Jorgensen, W. et al. Comparison of simple potential functions for simulating liquid water. *J. Chem. Phys.* **79**, 926–935 (1983).

62. Feller, S. et al. Constant pressure molecular dynamics simulation: the Langevin piston method. *J. Chem. Phys.* **103**, 4613–4621 (1995).

63. Phillips, J. et al. Scalable molecular dynamics on CPU and GPU architectures with NAMD. *J. Chem. Phys.* **153**, 44130 (2020).

64. Darden, T., York, D. & Pedersen, L. Particle mesh Ewald: An N· log (N) method for Ewald sums in large systems. *J. Chem. Phys.* **98**, 10089–10092 (1993).

65. Frishman, D. & Argos, P. Knowledge-based protein secondary structure assignment. *Proteins Struct. Funct. Bioinform.* **23**, 566–579 (1995).

Acknowledgements

Author contributions

D.K., C.L. and Y.W. conceived the idea and designed the research. Y.W., J.W., R.M., J.S., C.C. and C.J conducted experiments for materials preparation and their characterization. Y.W., X.L. and Y.C. performed cell experiments. W.H. conducted SSNMR characterization of the materials. Y.W., J.W., and E.H. performed bacterial cultures. Y.W., B.L. and C.L. conducted in vivo studies, histological analysis and discussed the results. Y.W., D.K., and C.L. wrote the manuscript. D.K., and C.L. supervised the research. All authors discussed and commented on the data.

Competing interests

The authors declare no competing interests.

Additional information

Supplementary information The online version contains supplementary material available at https://doi.org/10.1038/s41467-024-55097-x.

Correspondence and requests for materials should be addressed to Chunmei Li or David L. Kaplan.

Peer review information *Nature Communications* thanks Hendrik Bargel, and the other, anonymous, reviewer(s) for their contribution to the peer review of this work. A peer review file is available.

Reprints and permissions information is available at http://www.nature.com/reprints

Publisher's note Springer Nature remains neutral with regard to jurisdictional claims in published maps and institutional affiliations.